Journal of Materials Chemistry A

Accepted Manuscript

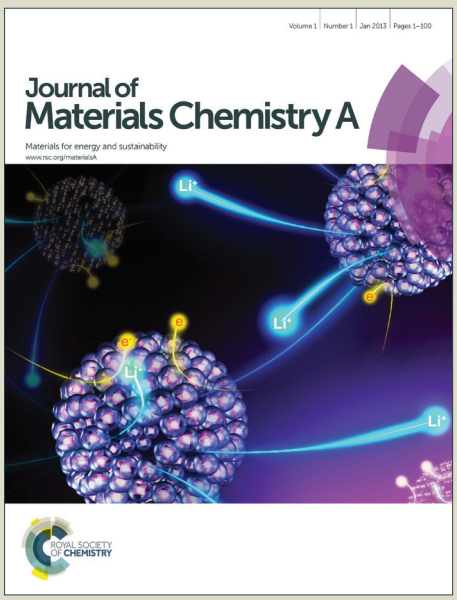

ROYAL SOCIETY OF CHEMISTRY

www.rsc.org/materialsA

TOC Graphics

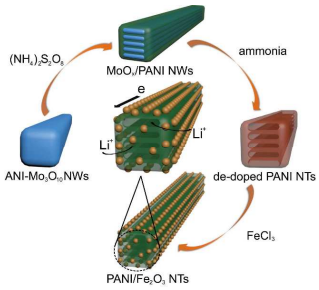

A Fe_2O_3-decorated polyaniline multi-channeled nanotube structure is synthesized for aqueous rechargeable lithium-ion battery anode, with superior cycling performance.

Journal Name

RSCPublishing

ARTICLE

Aqueous Li-ion Cells with Superior Cycling Performance Using Multi-channeled Polyaniline/Fe_2O_3 Nanotube Anodes

Cite this: DOI: 10.1039/xoxxoooooox

Received ooth January 2012,
Accepted ooth January 2012

DOI: 10.1039/xoxxoooooox

www.rsc.org/

Yuhang Wang,[a] Yehua Wang,[a] Jing Tang,[a] Yongyao Xia,[a] and Gengfeng Zheng*[a]

We developed a Fe_2O_3-decorated polyaniline (PANI/Fe_2O_3) multi-channeled nanotube structure as aqueous rechargeable lithium-ion battery (ARLIB) anode, using polymerized aniline-Mo_3O_{10} (ANI-Mo_3O_{10}) nanowires as the template. The removal of MoO_x from the intercalated layered MoO_x/PANI structures results in a multi-channeled nanotube structure, and the subsequent hydrothermal growth of Fe_2O_3 nanoparticles on PANI surface can simultaneously re-dope PANI into a highly conductive form. The multi-channeled nanotube structure allows for sufficient electrolyte impregnation and efficient one-dimensional electron transport, and the decorated Fe_2O_3 surface layer offers a much extended voltage window of the electrode and improves the chemical and electrochemical stability. As a proof-of-concept, the initial discharge and charge capacities of the PANI/Fe_2O_3 multi-channeled nanotube anode are 60.5 and 54.2 mA h g^{-1} at a current rate of 150 mA g^{-1}, respectively. When fabricated as a full ARLIB cell with the PANI/Fe_2O_3 multi-channeled nanotube anode and a $LiMn_2O_4$ cathode, an initial discharge capacity of 50.5 mA h g^{-1} is obtained at the current rate of 150 mA g^{-1}, with superior capacity retention of 73.3% after over 1000 charge/discharge cycles.

Introduction

The aqueous rechargeable lithium-ion batteries (ARLIBs) have been capturing substantial attention worldwide since its first development as the VO_2(B)//$LiMn_2O_4$ system in 1994.[1] Attributed to their non-inflammable property, high conductivity and abundant source of aqueous electrolyte,[2] ARLIBs are potential to circumvent the safety and cost problems associated with the non-aqueous Li-ion batteries.[3-8] Nonetheless, due to the constraints of complicated chemical and electrochemical processes possibly taking place in aqueous systems, including electrode materials side-reactions with water or oxygen,[2] proton co-intercalation[9] and water splitting,[10] the VO_2(B)//$LiMn_2O_4$ system[1] and the following works[11, 12] mostly presented poor capacity retentions (< 50% after 100 cycles). To date, only a limited number of electrode materials, such as active carbon,[13] vanadium oxides,[14] lithium vanadium oxides,[11] and NASICON-$LiTi_2(PO_4)_3$[15], have been demonstrated for the ARLIB anodes.

Recently, conductive polymers such as polyaniline (PANI) and polypyrrole (PPy) have also been suggested as ARLIB anodes, due to their low solubility and high conductivity in aqueous solution.[16, 17] The charging/discharge mechanism is based on the doping/de-doping of anions in these electrode materials, while their voltage windows for ARLIB cells are still low.[18, 19] On the other hand, iron oxide (Fe_2O_3) shows a higher net potential (–0.6 V v.s. Ag/AgCl) than PANI or PPy when explored as the negative electrode for asymmetric supercapacitors,[20] while the inherent poor electron conductivity still hinders its application as energy storage device with long-life cycle stability.[21] The combination of PANI and Fe_2O_3 may represent a rational candidate for the ARLIB anode, which has not been realized. Moreover, when fabricated as low-dimensional nanostructures with decreased diffusion length, enhanced kinetics, large pores and abundant ionic contact area,[22-27] this ARLIB design may allow for a much extended voltage window and superior cycling performance, which are also attributed to the conductive PANI, Fe_2O_3 with more negative redox potential, and their low solubilities in aqueous electrolyte.

Herein, we developed a synthetic approach of a Fe_2O_3-decorated multi-channeled PANI (PANI/Fe_2O_3) nanotube (NT) structure using layered MoO_3 nanobelts as templates, and its application for ARLIBs. The synthesis process is schematically displayed in **Fig. 1**. The aniline-Mo_3O_{10} (ANI-Mo_3O_{10}) NWs with layered structures are first synthesized as the growth template, based on the previous report.[28] The PANI-intercalated MoO_x (MoO_x/PANI) NWs are then obtained via the redox polymerization reaction between ANI^+ ions and ammonium persulfate (APS) in hydrochloride acid (Experimental section). Afterwards, the MoO_x is etched away by the treatment of ammonia water ($NH_3 \cdot H_2O$), during which PANI is also de-doped. The Fe_2O_3-decorated multi-channeled PANI NTs are further obtained in a $FeCl_3$ aqueous solution under a hydrothermal condition. The acidic property and hydrolysis of Fe^{3+} can simultaneously deposit Fe_2O_3 nanoparticles on the PANI polymer frameworks and re-dope the intrinsic PANI to achieve excellent electrical conductivity. The multi-channeled NT structure is beneficial for sufficient electrolyte impregnation and electron transport, as well as structure stability. As a proof-of-concept, ARLIB full cells using the PANI/Fe_2O_3 NTs and $LiMn_2O_4$ as anode and cathode, respectively, show a much enhanced cycling stability. An initial discharge capacity of 50.5 mA h g^{-1} is obtained at a current

density of 150 mA g^{-1} based on the weight of the anode material, and the capacity retention is 73.3% (37.1 mA h g^{-1}) after more than 1000 cycles.

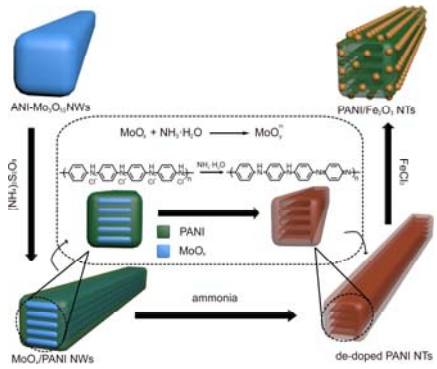

Figure 1. Schematic illustration of the synthesis procedure of the Fe_2O_3-decorated PANI multi-channeled (PANI/Fe_2O_3) NTs.

Experimental

Synthesis of aniline-Mo_3O_{10} nanowires (ANI-Mo_3O_{10} NWs)

In typical process, 2.48 g of $(NH_4)_6Mo_7O_{24}{\cdot}4H_2O$ and 3.44 g of distilled aniline monomer were dissolved in 40 mL of deionized (DI) water. Then a hydrochloride acid solution (1 M) was added dropwise under stirring until a white precipitate appeared. The mixture was transferred into a water bath and kept at 50 °C for 2 h under vigorous stirring. The white product was filtered and dried at 60 °C under vacuum.

Synthesis of MoO_x/polyaniline nanowires (MoO_x/PANI NWs)

MoO_x/PANI NWs were synthesized via an in-situ polymerization process. 0.68 g of ANI-Mo_3O_{10} NWs were dispersed into 80 mL of DI water by ultrasonication, and 0.57 g of $(NH_4)_2S_2O_8$ was slowly added into the mixture with magnetic stirring. The solution pH was adjusted to ~2 by hydrochloride acid (1 M). After stirring for 6 h, black-green powder was collected by filtration and dried at 60 °C under vacuum.

Synthesis of Fe_2O_3-decorated PANI (PANI/Fe_2O_3) multi-channeled nanotubes

The MoO_x/PANI NWs were dispersed into 1 M ammonia, filtered and dried after 2 h to get de-doped PANI NTs. The de-doped PANI NTs were added into 40 mL of $FeCl_3{\cdot}6H_2O$ solution (0.02 M) under stirring. The mixture was transferred into a 50-mL autoclave and kept at 100 °C for 2 h. The PANI/Fe_2O_3 multi-channeled NTs were obtained by centrifugation and dried at 60 °C under vacuum. The re-doped PANI NTs were made by dispersing the de-doped samples into hydrochloride acid (1 M).

Electrochemical measurements

The electrochemical performances of the PANI/Fe_2O_3 NTs were investigated using a simulated lithium-ion cell. The anode was made by mixing of the PANI/Fe_2O_3 NTs, carbon black (acetylene black) and polytetrafluoroethylene (PTFE, Aldrich Co.), in a weight ratio of 80:10:10 and manually rolled into a thin film in a roller machine. The commercial $LiMn_2O_4$ electrode was used as the cathode. The stainless steel grid and porous paper were used as the current collector and separator, respectively. The electrode was compressed on to the stainless steel grid at 30 MPa and dried at 120 °C in air for 12 h. The mass loadings of anode and cathode are 3.6 and 2.0 mg cm^{-2}, respectively. A Li_2SO_4 (0.5 M) aqueous solution was used as the electrolyte. For half-cell cyclic voltammetry measurement, a 3-electrode cell was employed, in which PANI/Fe_2O_3 NTs or commercial $LiMn_2O_4$ was used as working electrode, and an Ag/AgCl electrode and active carbon were used as reference and counter electrodes, respectively. The half cells and full cells were tested using a CHI660D electrochemical workstation (CHI Inc., USA).

Results and discussion

Scanning electron microscopy (SEM) images show the ANI-Mo_3O_{10} NWs are ~200 nm in width and several microns in length, and agglomerate with each other (**Fig. S1a**). After the electro-polymerization of PANI, the MoO_x/PANI NWs exhibit a NW structure with rough surface, which is well retained in the following synthesis processes (**Fig. S1b-d**). The high resolution SEM images show that the surfaces of PANI become relatively smooth (**Fig. 2a**). Distinct from the PANI without Fe_2O_3 deposition (**Fig. S2a-c**), a layer of nanoparticles is clearly observed on the surface of the PANI/Fe_2O_3 nanocomposites after the Fe_2O_3 growth (**Fig S2d-f**). The deposition layer is nanocrystalline with an average size less than 5 nm (**Fig. 2b**). Transmission electron microscopy (TEM) images reveal the multi-channeled tubular structures of the re-doped PANI and PANI/Fe_2O_3 nanocomposites (**Fig. 2c, d**). The fringes with different contrasts on a single NT indicate the multi-channeled structure, and the number of channels of each NT is ranged from 2 to 5. The energy dispersive spectroscopy (EDS) mapping confirms the Fe_2O_3-decorated PANI NT structure (**Fig. S3a-e**). The complete removal of Mo and the formation of Fe_2O_3 are also exhibited by the EDS data (**Fig. S3, g**), consistent with the mapping results.

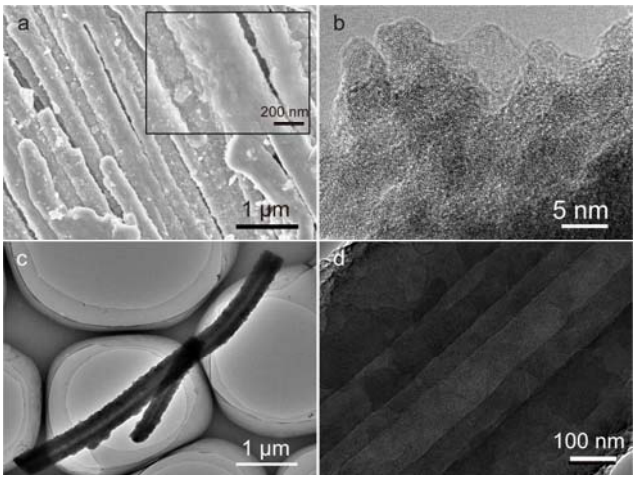

Figure 2. (a) SEM images of PANI/Fe_2O_3 NTs. Inset: NT surface at higher magnifications. (b) High-resolution TEM images of the surface Fe_2O_3 nanoparticles. (c) TEM images of a representative re-doped PANI NT. (d) Zoom-in image of the NT in c, showing 5 inner channels.

The X-ray diffraction (XRD) pattern of the ANI-Mo_3O_{10} (**Fig. S4**) confirms the template is monoclinic $Mo_3O_{10}(C_6H_8N)_2{\cdot}2H_2O$ (JCPDS

No. 50-2402). For the MoO_x/PANI NWs, the wide peak located at the range of 5 to 10 degrees in the XRD pattern corresponds to the *d*-spacing value of 1.32 nm, suggesting the intercalation of PANI into MoO_x layers (**Fig. 3a**, purple curve).[29] As for the de-doped PANI, re-doped PANI and PANI/Fe_2O_3 (**Fig. 3a**, green, blue and red curves), the diffraction peaks are still retained with decreased intensities, which may indicate the multi-channeled structure after the removal of MoO_x. For the MoO_x/PANI, re-doped PANI, and PANI/Fe_2O_3, the three wide successive peaks from 15 to 30 degrees are ascribed to the formation of the quaternary ammonium type N atoms after the HCl doping, while only one wide peak is presented at the same region for de-doped PANI because of its emeraldine base (EB) form property.[30] The infra-red (IR) spectra of these samples are further displayed (**Fig. 3b**). For ANI-Mo_3O_{10} (black curve), the absorption band around 3080 and 2900 cm^{-1} are ascribed to the ν_{C-H} in benzene ring. The peaks at 1580 and 1480 cm^{-1} can be assigned to the characteristic of benzene ring.[28] The band located at 2580 and 1120 cm^{-1} are attributed to ν_{NH3+} and ν_{C-N}, respectively.[28] For all other samples, the band at 1580 and 1470 cm^{-1} correspond to the stretching vibrations of quinonoid (Q-type) and benzenoid (B-type) rings, respectively. The peaks at 1300 and 1240 cm^{-1} are assigned to the ν_{C-N} in Q-B-Q structures and B-type rings. The peaks at 1150 and 830 cm^{-1} are attributed to the band vibrations inside and outside the faces of B-type rings, respectively (**Fig. 3b**, red curve). These results indicate the successful synthesis of PANI and its existence in subsequent steps.

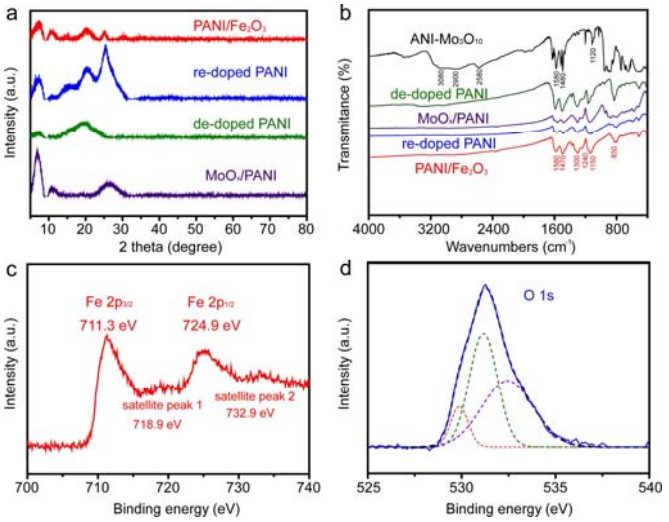

Figure 3. (a) XRD patterns of MoO_x/PANI NWs, de-doped PANI NTs, re-doped PANI NTs, and PANI/Fe_2O_3 NTs, respectively. (b) Fourier-transformed IR spectra of ANI-Mo_3O_{10} NWs, MoO_x/PANI NWs de-doped PANI NTs, re-doped PANI NTs, and PANI/Fe_2O_3 NTs. (c) Fe 2p and (d) O 1s XPS spectra collected from the PANI/Fe_2O_3 multi-channeled NTs. The fitting results of the O 1s spectrum are displayed in dotted lines.

The presence of Fe_2O_3 in the multi-channeled PANI/Fe_2O_3 NTs is further confirmed by the X-ray photoelectron spectroscopy (XPS, **Fig. 3c, d**). Two peaks at 711.3 and 724.9 eV are observed, corresponding to the Fe $2p_{3/2}$ and Fe $2p_{1/2}$.[20] The small peaks at 718.9 and 732.9 eV are attributed to the satellite peaks of Fe $2p_{3/2}$ and Fe $2p_{1/2}$, respectively.[31] The O 1s spectrum can be disassembled into three peaks centered at 529.9, 531.2, and 532.5 eV (**Fig. 3d**, dotted lines), corresponding to the binding energies of Fe-O, Fe-OH and absorbed oxygen, respectively.[32] The porosity of PANI/Fe_2O_3 NTs is characterized by N_2 sorption, which shows a typical type-*IV* isotherm (**Fig. S5a**), suggesting a mesoporous structure of the NTs. The Brunauer-Emmett-Teller (BET) specific surface area of the PANI/Fe_2O_3 NTs is 15.3 m^2 g^{-1}, with a relatively narrow Barrett-Joyner-Halenda (BJH) pore size distribution and an average pore size of 4.0 nm (**Fig. S5b**), attributed to the removal of MoO_x as well as the particle stacking.

The electrochemical properties of both the multi-channeled PANI/Fe_2O_3 NTs and commercial $LiMn_2O_4$ were first tested in a standard 3-electrode design (Experimental section). Cyclic voltammetry (CV) spectroscopies of PANI/Fe_2O_3 and commercial $LiMn_2O_4$ are exhibited to show the chemical reactions of each electrode during charge/discharge process **(Fig. 4a)**. For PANI/Fe_2O_3 (red curve), the CV curves measured between 0.5 V to –0.9 V (v.s. Ag/AgCl) at a scan rate of 1 mV s^{-1} show two pairs of anodic and cathodic peaks. The pair of wide redox peaks located at ~ –0.5 V is associated with the reversible reaction of Fe^{3+}/Fe^{2+} couple.[20] The other pair of peaks at ~ 0 V is assigned to the re-doping/de-doping process of anions such as Cl^- and SO_4^{2-}.[33] The irreversible behavior is caused by the side reaction with oxygen in the open three-electrode system.[2] For $LiMn_2O_4$ (black curve), the wide anodic peak from 0.8 to 1.4 V (vs. Ag/AgCl) at the same scan rate is attributed to the de-intercalation of Li^+ at the available tetrahedron sites, and the cathodic one shows the reverse process.[34]

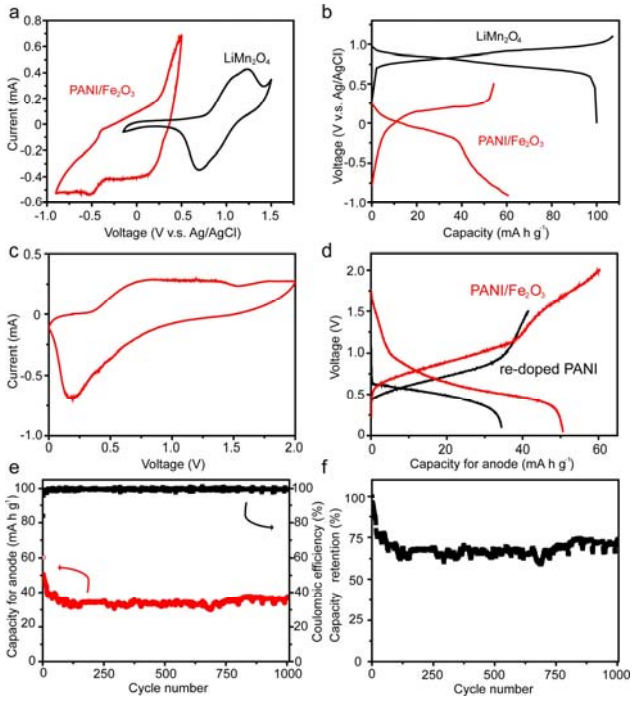

Figure 4. (a) Cyclic voltammetry spectra of the PANI/Fe_2O_3 NTs and commercial $LiMn_2O_4$ in the first cycle at a scanning rate of 1 mV s^{-1}. (b) Initial charge and discharge curves of the PANI/Fe_2O_3 NTs and commercial $LiMn_2O_4$ at a current rate of 100 mA g^{-1}. (c) Cyclic voltammetry spectra of the ARLIB, which is assembled by using PANI/Fe_2O_3 and commercial $LiMn_2O_4$ as anode and cathode, in the first cycle at the scanning rate of 1 mV s^{-1}. (d) Initial charge and discharge curves of the (PANI/Fe_2O_3)//$LiMn_2O_4$ ARLIB full cell, at a current rate of 150 mA g^{-1}. The calculated specific capacities are based on the mass of active materials for anode. (e) Cycling performance (left *y*-axis) and Coulombic efficiency (right *y*-axis) of the (PANI/Fe_2O_3)//$LiMn_2O_4$ ARLIB full cell at a current rate of 150 mA g^{-1} for 1000 cycles. (f) Capacity retention of the (PANI/Fe_2O_3)//$LiMn_2O_4$ ARLIB full cell.

The charges/discharge curves of PANI/Fe_2O_3 and $LiMn_2O_4$ are subsequently displayed (**Fig. 4b**). The voltage windows of the anode and cathode are determined based on the results of the CV measurements. The initial discharge and charge capacities of PANI/Fe_2O_3 are 60.5 and 54.2 mA h g^{-1} at a current rate of 150 mA g^{-1}, with a Coulombic efficiency of ~90% (**Fig. 4b**, red curve). The charge and discharge capacitance of $LiMn_2O_4$ are ~107 and 100 mA h g^{-1} at a current rate of 300 mA g^{-1}, respectively (**Fig. 4b**, black curve).

The electrochemical performances of the ARLIB full cell employing the PANI/Fe_2O_3 multi-channeled NTs and commercial $LiMn_2O_4$ as anode and cathode, respectively, (in a weight ratio of 1.8:1), are investigated using a 2-electrode simulated cell design (Experimental section). The CV curves of the (PANI/Fe_2O_3)//$LiMn_2O_4$ full cell show the complete reactions during the charge/discharge processes (**Fig. 4c**), which are involved with the de-intercalation/intercalation of Li^+, de-doping/re-doping of anions, and the reversible redox reaction of Fe^{3+}/Fe^{2+}. The voltage window of the full cell is determined according to the charge/discharge curves of the anode and cathode, and the redox potentials of $LiMn_2O_4$ PANI and Fe_2O_3 have to be contained in this range. At a voltage window between 2.0 and 0.05 V and a current rate of 150 mA g^{-1}, the initial charge and discharge capacities (based on the weight of anode active materials) are measured as 60.3 and 50.5 mA h g^{-1}, respectively, with a Coulombic efficiency of ~84% (**Fig. 4d**). The capacity decay in the first 20 cycles may be due to some irreversible reactions between the active materials and the electrolyte. The reversible capacity is retained at 37.1 mA h g^{-1} for the anode (~ 67 mA h g^{-1} for the cathode) after more than 1000 cycles, with a high capacity retention of 73.3% (**Fig. 4e, f**), comparable with the best ARLIB full cells reported previously.[2, 16] Moreover, the capacity loss from 20 to 1000 cycles is nearly negligible, indicating the superior cyclic performance of the ARLIB. For comparison, the initial charge/discharge curve of the re-doped PANI//$LiMn_2O_4$ full cell is also displayed (**Fig. 4c**, black curve), and the voltage window is selected to be ranged from 1.5 to 0.05 V, based on the previous report.[18] The discharge curve of the re-doped PANI//$LiMn_2O_4$ full cell presents a sharply drop from 1.0 to 0.6 V which can be attributed to the absence of Fe_2O_3, and the reversible capacity is only ~25 mA h g^{-1} after 40 charge/discharge cycles (**Fig. S6a**, black curve), substantially lower than the ARLIB full cells consisting of multi-channeled PANI/Fe_2O_3 NT anodes. The reversible capacity of the (PANI/Fe_2O_3)//$LiMn_2O_4$ full cell (based on the weight of anode materials) is ~33 mA h g^{-1} at the current rate of 1.5 A g^{-1}, and recovers to ~50 mA h g^{-1} when the current reset to 0.15 A g^{-1} (**Fig. S6b**), exhibiting a good rate cyclic performance.

For a more comprehensive comparison, the electrochemical performances of the MoO_x/PANI were also measured, as the Li^+ intercalation/de-intercalation potentials in MoO_x also meet the demand for the ARLIB application.[35] The initial charge/discharge curve of (MoO_x/PANI)//$LiMn_2O_4$ full cell measured at the range of 1.4 to 0.05 V is displayed (**Fig. S7a**), while the capacity and the cycle stability are still lower than the multi-channeled PANI/Fe_2O_3 NT anodes (**Fig. S7b**), ascribed to the dissolution of MoO_x in the aqueous electrolyte.[35] Further increasing the upper voltage limit to 1.85 V leads to a much worse electrochemical performance degradation, suggesting the occurrence of more severe electrode dissolution and irreversible electrochemical reactions. In contrast, the Coulombic efficiency of the multi-channeled (PANI/Fe_2O_3)//$LiMn_2O_4$ full cell from the third to the 1000th cycles always remains > 98%, suggesting a large hydrogen evolution overpotential of PANI/Fe_2O_3, high reversibility of the electrochemical process and the superior cyclic capability (**Fig. 4e**, black curve).

To further interrogate the extraordinary cycling performance of the multi-channeled PANI/Fe_2O_3 NT anode, the morphology retention of the electrode was evaluated after electrochemical tests. The SEM images of the electrode after 70 discharge/charge cycles present a well preserved 1D nanostructure, compared to that of electrode prior to cycling (**Fig. S8a, b**). Furthermore, the capacity fading induced by the electrode dissolution is examined by the color change of the separators after 10 charge/discharge cycles. For the re-doped PANI NTs and MoO_x/PANI NWs, the green color of the separators suggests that the capacity fading is mainly caused by the dissolution of the active materials. While for the multi-channeled PANI/Fe_2O_3 NTs, the separator still shows a white color after repeated discharge/charge cycles, which can be attributed to the high stability of the Fe_2O_3 surface layer (**Fig. S8c**). Moreover, the multi-channeled NTs structure and existence of mesopores can improve the electrolyte impregnation. The 1D PANI frameworks provide efficient electron transfer, and PANI/Fe_2O_3 can extend the voltage window of the ARLIB and prevent the dissolution of the active materials. Together with the electrochemical performances of the (PANI/Fe_2O_3)//$LiMn_2O_4$ ARLIB full cells, these results confirm our rational design for using multi-channeled Fe_2O_3-decorated PANI NTs as the anode materials for ARLIBs.

Conclusions

In summary, we have developed a facile two-step etching/doping process for synthesis of multi-channeled PANI/Fe_2O_3 NTs as ARLIB anodes, using an aniline-Mo_3O_{10} (ANI-Mo_3O_{10}) NWs as the template. The in-situ polymerization of ANI^+ of the ANI-Mo_3O_{10} NWs results in an intercalated layered structure of MoO_x/PANI NWs, in which MoO_x is etched by to form multi-channeled NT structure, which allows for sufficient electrolyte impregnation and efficient 1D electron transport pathways. Further growth of Fe_2O_3 nanoparticles on PANI surface can extend the voltage window of the electrode as well as increase the electrode stability. The PANI/Fe_2O_3 NTs also provide a large hydrogen evolution overpotential that is beneficial for a high coulombic efficiency of the full cell. The initial discharge and charge capacities of PANI/Fe_2O_3 NTs are 60.5 and 54.2 mA h g^{-1} at a current rate of 150 mA g^{-1}. When measured as the anode in an ARLIB full cell using $LiMn_2O_4$ as cathode, it exhibits an initial discharge capacity of 50.5 mA h g^{-1} at a current rate of 150 mA g^{-1}, based on the weight of the anode material, and a superior capacity retention is 73.3% (37.1 mA h g^{-1}) after over 1000 charge/discharge cycles. Further optimization of the composition and loading amount of the metal oxides, as well as the nanostructure design and fabrication, may allow for more material architectures and device concepts that lead to a promising ARLIB energy storage device with low cost, safety, high energy and power densities.

Acknowledgements

We thank the following funding agencies for supporting this work: the National Key Basic Research Program of China (2013CB934104), the Natural Science Foundation of China (21322311, 21473038, 21071033), the Science and Technology Commission of Shanghai Municipality (14JC1490500), the Doctoral Fund of Ministry of Education of China (20130071110031), the Program for Professor of Special Appointment (Eastern Scholar) at Shanghai Institutions of Higher Learning, and the Deanship of Scientific Research of King Saud University (IHCRG#14-102).

Notes and references

[a] Laboratory of Advanced Materials, Department of Chemistry, Fudan University, Shanghai, 200433, People's Republic of China. E-mail: gfzheng@fudan.edu.cn.

† Electronic Supplementary Information (ESI) available: [More SEM images, other structure characterizations and electrochemical test]. See DOI: 10.1039/b000000x/

1 W. Li, J. R. Dahn, D. S. Wainwright, *Science* 1994, **264**, 1115.
2 J. Y. Luo, W. J. Cui, P. He, Y. Y. Xia, *Nat. Chem.* 2010, **2**, 760.
3 J. M. Tarascon, M. Armand, *Nature* 2001, **414**, 359.
4 P. G. Bruce, B. Scrosati, J. M. Tarascon, *Angew. Chem. Int. Ed.* 2008, **47**, 2930.
5 G. Zhang, X. W. D. Lou, *Angew. Chem. Int. Ed.* 2014, **53**, 9041.
6 X. Lai, J. E. Halpert, D. Wang, *Energy Environ. Sci.* 2012, **5**, 5604.
7 X. Rui, X. Zhao, Z. Lu, H. Tan, D. Sim, H. H. Hng, R. Yazami, T. M. Lim, Q. Yan, *Acs Nano* 2013, **7**, 5637.
8 Y. Wang, G. Z. Cao, *Adv. Mater.* 2008, **20**, 2251.
9 Q. Shu, L. Chen, Y. Y. Xia, X. G. Gong, X. Gu, *J. Phys. Chem. C* 2013, **117**, 6929.
10 Y. G. Wang, J. Yi, Y. Y. Xia, *Adv. Energy Mater.* 2012, **2**, 830.
11 G. J. Wang, L. J. Fu, N. H. Zhao, L. C. Yang, Y. P. Wu, H. Q. Wu, *Angew. Chem. Int. Ed.* 2007, **46**, 295.
12 H. B. Wang, K. L. Huang, Y. Q. Zeng, S. Yang, L. Q. Chen, *Electrochimi. Acta* 2007, **52**, 3280.
13 Y. G. Wang, Y. Y. Xia, *Electrochem. Commun.* 2005, **7**, 1138.
14 C. Z. Wu, Z. P. Hu, W. Wang, M. A. Zhang, J. L. Yang, Y. Xie, *Chem. Commun.* 2008, **33**, 3891.
15 J. Y. Luo, Y. Y. Xia, *Adv. Funct. Mater.* 2007, **17**, 3877.
16 W. Tang, X. W. Gao, Y. S. Zhu, Y. B. Yue, Y. Shi, Y. P. Wu, K. Zhu, *J. Mater. Chem.* 2012, **22**, 20143.
17 H. B. Wang, K. L. Huang, Y. Q. Zeng, F. G. Zhao, L. Q. Chen, *Electrochem. Solid State Lett.* 2007, **10**, A199.
18 L. Liu, F. H. Tian, M. Zhou, H. P. Guo, X. Y. Wang, *Electrochimi. Acta* 2012, **70**, 360.
19 G. J. Wang, L. C. Yang, Q. T. Qu, B. Wang, Y. P. Wu, R. Holze, *J. Solid State Electrochem.* 2010, **14**, 865.
20 P. H. Yang, Y. Ding, Z. Y. Lin, Z. W. Chen, Y. Z. Li, P. F. Qiang, M. Ebrahimi, W. J. Mai, C. P. Wong, Z. L. Wang, *Nano Lett.* 2014, **14**, 731.
21 H. Wu, M. Xu, Y. C. Wang, G. F. Zheng, *Nano Research* 2013, **6**, 167.
22 C. K. Chan, H. Peng, G. Liu, K. McIlwrath, X. F. Zhang, R. A. Huggins, Y. Cui, *Nat. Nanotechnol.* 2008, **3**, 31.
23 L. Q. Mai, F. Yang, Y. L. Zhao, X. Xu, L. Xu, Y. Z. Luo, *Nat. Commun.* 2011, **2**, 381.
24 Y. H. Wang, Y. H. Wang, D. S. Jia, Z. Peng, Y. Y. Xia, G. F. Zheng, *Nano lett.* 2014, **14**, 1080.
25 D. Chao, X. Xia, J. Liu, Z. Fan, C. F. Ng, J. Lin, H. Zhang, Z. X. Shen, H. J. Fan, *Adv. Mater.* 2014, **26**, 5794.
26 B. Liu, J. Zhang, X. Wang, G. Chen, D. Chen, C. Zhou, G. Shen, *Nano Lett.* 2012, **12**, 3005.
27 X. L. Zhang, F. Y. Cheng, J. G. Yang, J. Chen, *Nano Lett.* 2013, **13**, 2822.
28 Q. S. Gao, S. N. Wang, H. C. Fang, J. W. Weng, Y. H. Zhang, J. J. Mao, Y. Tang, *J. Mater. Chem.* 2012, **22**, 4709.
29 L. C. Yang, S. N. Wang, J. J. Mao, J. W. Deng, Q. S. Gao, Y. Tang, O. G. Schmidt, *Adv. Mater.* 2013, **25**, 1180.
30 J. P. Pouget, M. E. Jozefowicz, A. J. Epstein, X. Tang, A. G. Macdiarmid, *Macromolecules* 1991, **24**, 779.
31 T. Yamashita, P. Hayes, *Appl. Surf. Sci.* 2008, **254**, 2441.
32 E. McCafferty, J. Wightman, *Surf. Interf. Anal.* 1998, **26**, 549.
33 J. J. Xu, K. Wang, S. Z. Zu, B. H. Han, Z. X. Wei, *Acs Nano* 2010, **4**, 5019.
34 W. Liu, G. Farrington, F. Chaput, B. Dunn, *J. Electrochem. Soc.* 1996, **143**, 879.
35 W. Tang, L. Liu, Y. Zhu, H. Sun, Y. Wu, K. Zhu, *Energy Environ. Sci.* 2012, **5**, 6909.